

Deciphering Interfacial Chemical and Electrochemical Reactions of Sulfide-Based All-Solid-State Batteries

Changhong Wang, Sooyeon Hwang, Ming Jiang, Jianwen Liang, Yipeng Sun, Keegan Adair, Matthew Zheng, Sankha Mukherjee, Xiaona Li, Ruying Li, Huan Huang, Shangqian Zhao, Li Zhang, Shigang Lu, Jiantao Wang, Chandra Veer Singh,* Dong Su,* and Xueliang Sun*

Large interfacial resistance resulting from interfacial reactions is widely acknowledged as one of the main challenges in sulfide electrolytes (SEs)-based all-solid-state lithium batteries (ASSLBs). However, the root cause of the large interfacial resistance between the SEs and typical layered oxide cathodes is not fully understood yet. Here, it is shown that interfacial oxygen loss from single-crystal $\text{LiNi}_{0.5}\text{Mn}_{0.3}\text{Co}_{0.2}\text{O}_2$ (SC-NMC532) chemically oxidizes $\text{Li}_{10}\text{GeP}_2\text{S}_{12}$, generating oxygen-containing interfacial species. Meanwhile, the interfacial oxygen loss also induces a structural change of oxide cathodes (layered-to-rock salt). In addition, the high operation voltage can electrochemically oxidize SEs to form non-oxygen species (e.g., polysulfides). These chemically and electrochemically oxidized species, together with the interfacial structural change, are responsible for the large interfacial resistance at the cathode interface. More importantly, the widely adopted interfacial coating strategy is effective in suppressing chemically oxidized oxygen-containing species and mitigating the coincident interfacial structural change but is unable to prevent electrochemically induced non-oxygen species. These findings provide a deeper insight into the large interfacial resistance between the typical SE and layered oxide cathodes, which may be of assistance for the rational interface design of SE-based ASSLBs in the future.

The success of ASSLBs could eventually eliminate the mileage anxiety and safety concerns of electric vehicles (EVs). To enable ASSLBs, various solid-state electrolytes have been intensively developed over the past decades, such as sulfide electrolytes (SEs),^[1b,c,2] oxide electrolytes,^[3] polymer-based electrolytes,^[4] and emerging solid-state halide electrolytes (Li_3MCl_6 , $\text{M} = \text{Y, In, Er, Sc, etc.}$).^[5] Owing to the high ionic conductivity and soft mechanical properties of SEs, it is widely believed that SE-based ASSLBs will be a leading contender for large-scale energy storage, particularly for the fast-growing industry of electric vehicles.

However, several challenges hinder the development of SE-based ASSLBs, including (1) moisture sensitivity and narrow electrochemical windows of SEs; (2) large interfacial resistance between electrodes and SEs that is caused by detrimental interfacial reactions; and (3) short-circuits when lithium dendrites penetrate through thin SE separators. In recent years, various SEs have been synthesized


with much-improved moisture stability, e.g., As-substituted Li_4SnS_4 ,^[6] Sb-doped $\text{Li}_{10}\text{GeP}_2\text{S}_{12}$,^[7] and $\text{Li}_{6.6}\text{Ge}_{0.6}\text{Sb}_{0.4}\text{S}_5\text{I}$.^[8] To fully realize the high energy density of ASSLBs, thin lithium metal is preferred, but lithium dendrite growth through the SE separator and SE reduction by Li metal needs to be addressed.

1. Introduction

All-solid-state lithium batteries (ASSLBs) have gained substantial attention owing to their higher energy density and excellent safety in comparison to current lithium-ion battery technology.^[1]

Dr. C. Wang, Dr. J. Liang, Y. Sun, K. Adair, M. Zheng, Dr. X. Li, R. Li, Prof. X. Sun
Department of Mechanical and Materials Engineering
University of Western Ontario
1151 Richmond St, London, Ontario N6A 3K7, Canada
E-mail: xsun9@uwo.ca

Dr. S. Hwang, Dr. D. Su
Center for Functional Nanomaterials
Brookhaven National Laboratory
Upton, NY 11973, USA
E-mail: dsu@bnl.gov

 The ORCID identification number(s) for the author(s) of this article can be found under <https://doi.org/10.1002/aenm.202100210>.

M. Jiang, Dr. S. Mukherjee, Prof. C. V. Singh
Department of Materials Science and Engineering
University of Toronto
Toronto, Ontario M5S 3E4, Canada
E-mail: chandraveer.singh@utoronto.ca

Dr. H. Huang
Glabat Solid-State Battery Inc.
700 Collip Circle, London, Ontario N6G 4X8, Canada

Dr. S. Zhao, Dr. L. Zhang, Dr. S. Lu, Dr. J. Wang
China Automotive Battery Research Institute Co., Ltd.
No. 11, Xingke East Street, Yanqi Economic Development Area,
Huairou District, Beijing 101407, China

DOI: 10.1002/aenm.202100210

Recently, Lee et al. demonstrated a high-energy-density (900 Wh L^{-1}) all-solid-state pouch cells with 1000 cycles based on a silver-carbon composite anode.^[1c] In terms of the cathode interface between typical high-voltage oxide cathodes and SEs, SE oxidation and decomposition have been widely reported and verified by validated by in situ X-ray photoelectron spectroscopy (XPS) and transmission electron microscopy (TEM).^[9] However, these acknowledged interfacial issues may be only partially responsible for the large interfacial resistance between SE and oxide cathodes.

In this work, we deciphered the initial trigger of interfacial reactions and revealed the associated near-surface structural change between single-crystal $\text{LiNi}_{0.5}\text{Mn}_{0.3}\text{Co}_{0.2}\text{O}_2$ (SC-NMC532) and sulfide electrolyte $\text{Li}_{10}\text{GeP}_2\text{S}_{12}$ (LGPS) by XPS, X-ray absorption spectroscopy (XAS), and high-resolution transmission electron microscopy (HRTEM). It was identified that interfacial oxygen loss from layered SC-NMC532 oxidizes SEs, generating oxygen species such as phosphates (PO_4^{3-}), sulfates (SO_4^{2-}), and sulfites (SO_3^{2-}) at the interface. Coincidentally, the interfacial oxygen loss induces an interfacial structural change of oxide cathodes from a layered structure to a rock-salt structure. Furthermore, it was found that the high operation voltage (2.5–4.4 V vs Li^+/Li) can electrochemically induce the formation of non-oxygen species such as polysulfides and elemental sulfur at the interface. These highly oxidized interfacial species in conjunction with interfacial structural change impede interfacial lithium-ion (Li^+) transport, thus leading to the large interfacial resistance of SE-based ASSLBs. More interestingly, the widely adopted interfacial coating strategy turns out to be

effective in suppressing interfacial oxygen loss and coincident local interfacial structural change of oxide cathodes but is unable to prevent the formation of electrochemically induced non-oxygen species (e.g., polysulfides, elemental S_8). To the best of our knowledge, this is the first time that the electrochemical and chemical reactions with the coincident interfacial structural change at the cathode/SE interface are separately discussed. These insightful understandings should help to rationally design the cathode toward high-performance SE-based ASSLBs.

2. Results

To obtain high-performance SE-based ASSLBs, highly Li^+ -conductive LGPS was chosen as the SE for this study. And single-crystal NMC532 was selected as the representative oxide cathodes owing to its particle integrity upon cycling, thus avoiding particle cracking influence. **Figure 1a–e** shows the STEM-EDX image and the Ni, Co, Mn, and O elemental maps of pristine SC-NMC532 with an average particle size of $3 \mu\text{m}$, demonstrating a homogenous distribution of all elements. Furthermore, an interfacial layer of $\text{LiNb}_{0.5}\text{Ta}_{0.5}\text{O}_3$ (LNTO) was coated on the SC-NMC532 (labeled as LNTO@SC-NMC532). The thickness of the conformal LNTO coating is 10 nm (Figure 1f). The STEM-EDX elemental maps of LNTO@SC-NMC532 show that Nb and Ta uniformly coated on the SC-NMC532 surface and Ta has a strong signal at the edge (Figure 1g–l), further validating that LNTO was uniformly coated on SC-NMC532. To confirm the interfacial stability

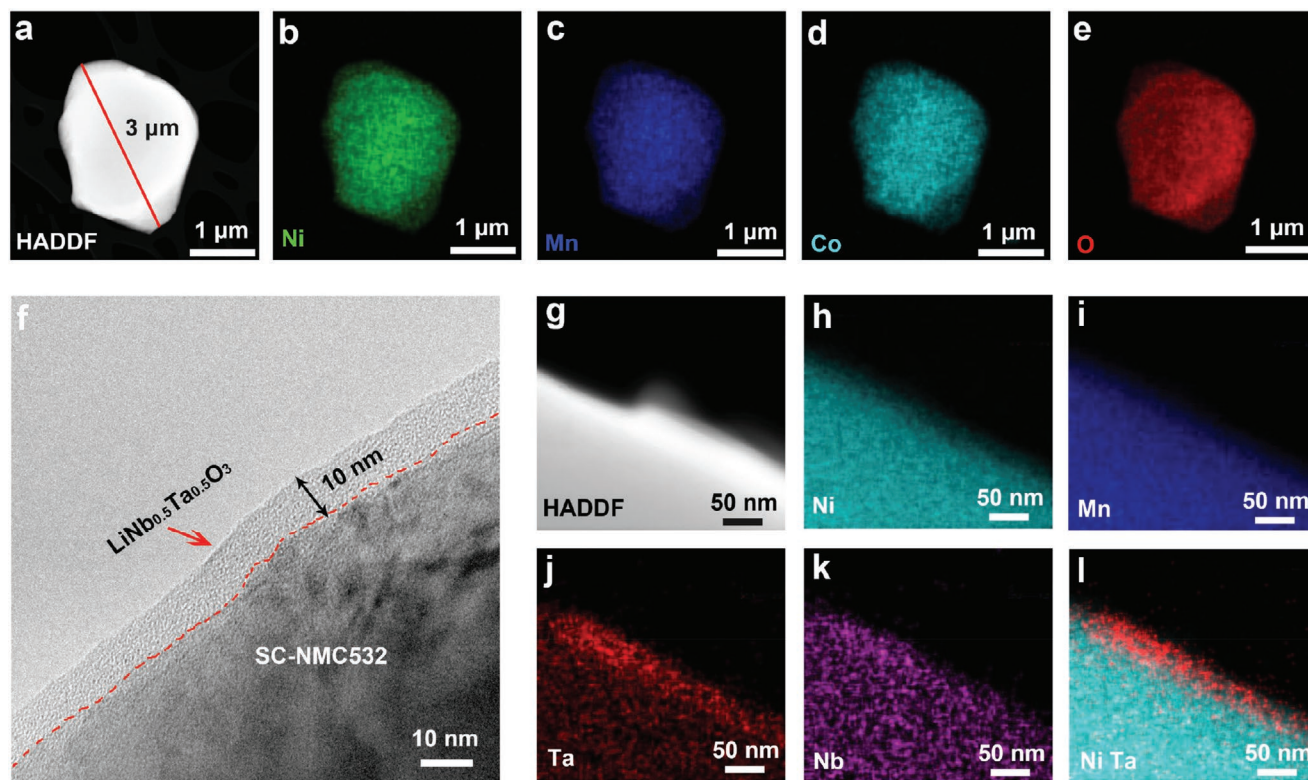


Figure 1. HRTEM images of pristine SC-NMC532 and LNTO@SC-NMC532. a) HAADF image of single-crystal NMC532. b) Ni, c) Mn, d) Co, and e) O elemental maps of SC-NMC532 acquired with STEM-EDX. f) Bright-field TEM image of $\text{LiNb}_{0.5}\text{Ta}_{0.5}\text{O}_3$ coating on SC-NMC532. g) HAADF image of LNTO@SC-NMC532. h) Ni, i) Mn, j) Ta, k) Nb, and l) a combination of Ni and Ta mapping results obtained from LNTO@SC-NMC532 with STEM-EDX.

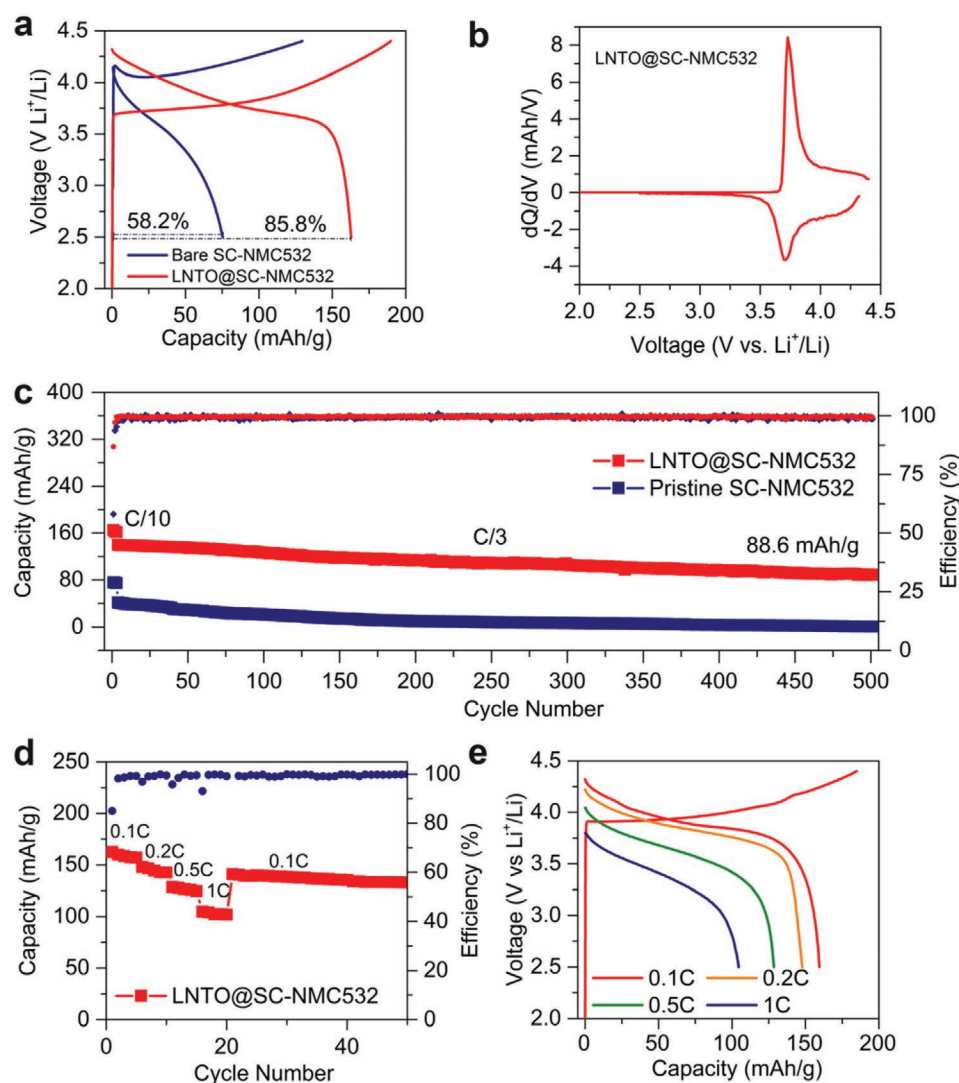


Figure 2. Electrochemical performance of pristine SC-NMC532 and LNT@SC-NMC532. a) Comparison of the charge/discharge curves of pristine SC-NMC532 and LNT@SC-NMC532. b) dQ/dV versus voltage. c) Cycling stability of pristine SC-NMC532 and LNT@SC-NMC532. d) Rate performance of LNT@SC-NMC532. e) Charge/discharge curves under different current densities.

between bare SC-NMC532, LNT, and LGPS, the interfacial reaction energies between bare SC-NMC532, LNT@SC-NMC532, and LGPS were calculated by the first-principles thermodynamic calculations (Figure S1, Supporting Information). The interface between SC-NMC532 and LGPS has poor stability, showing significant reaction energy of -0.38 eV/atom. In contrast, the interfacial reaction energy between LNT and LGPS is negligible (-0.08 eV/atom).^[10] This calculation validates that LNT is a stable interfacial coating material against LGPS.

The electrochemical performance of pristine SC-NMC532 and LNT@SC-NMC532 in SE-based ASSLBs was first tested under a current density of 0.1344 mA cm⁻² (0.1C). Bare SC-NMC532 can only be charged to 76.0 mAh g⁻¹ and discharged at 41.4 mAh g⁻¹ owing to the large overpotential caused by the significant interfacial reactions between SC-NMC532 and LGPS (Figure 2a). Comparatively, LNT@SC-NMC532 is charged to 188.2 mAh g⁻¹ and discharged at 161.4 mAh g⁻¹,

implying that the LNT interfacial coating can effectively suppress interfacial reactions. With the LNT interfacial coating, the initial Coulombic efficiency of 54.5% of bare SC-NMC532 increased to 85.8%, which approaches that of liquid-based cells (86.1%) (Figure S2, Supporting Information). The interfacial resistance between bare SC-NMC532 and LGPS is as large as 1400 Ω and was reduced to 248 Ω by a 10 nm LNT interfacial coating (Figure S3, Supporting Information), implying that interfacial coating is effective in suppressing the large interfacial resistance of ASSLBs.

Only one pair of reversible peaks was observed in the dQ/dV curve (Figure 2b), which hints at excellent structure stability of SC-NMC532 in ASSLBs.^[11] The structural stability of SC-NMC532 was also demonstrated by the excellent cycling stability of LNT@SC-NMC532 (Figure 2c). The discharge capacity of LNT@SC-NMC532 is 139.8 mAh g⁻¹ at C/3, which remains at 88.6 mAh g⁻¹ after 500 cycles at C/3, while

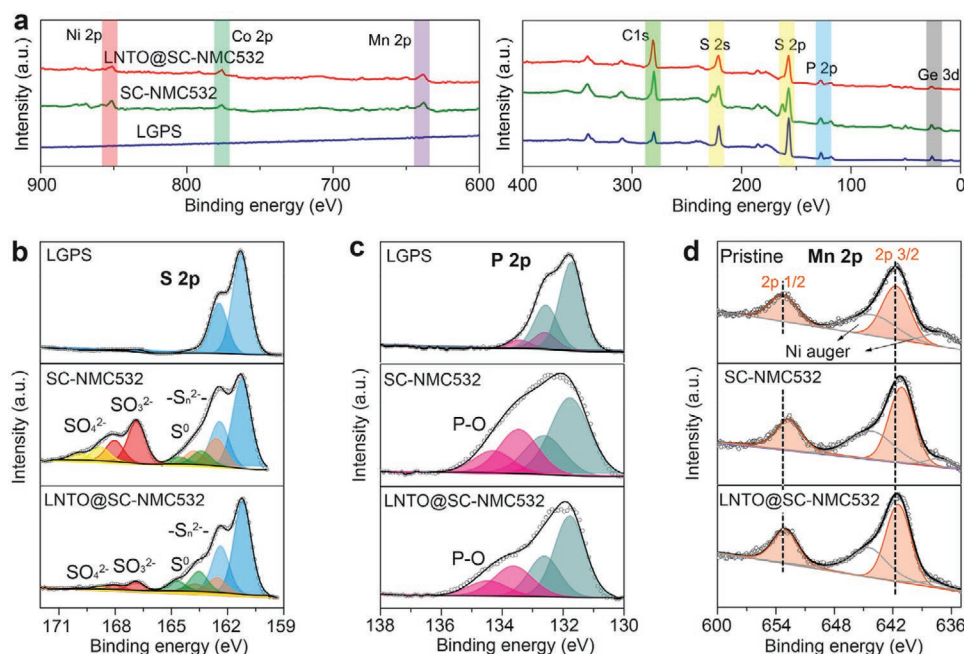


Figure 3. XPS spectra of LGPS, bare SC-NMC532/LGPS electrode after 100 cycles, and LNT@SC-NMC532 electrode after 100 cycles. a) Full survey, b) S 2p spectra, c) P 2p spectra, and d) Mn 2p spectra.

the discharge capacity of bare SC-NMC532 decays to zero after 200 cycles. The decay rate of LNT@SC-NMC532 is as low as $0.09\% \text{ cycle}^{-1}$. Figure 2d shows the rate performance of LNT@SC-NMC532 from 0.1 to 1C and the corresponding discharge curves are displayed in Figure 2e. LNT@SC-NMC532 shows a discharge capacity of 104.7 mAh g^{-1} at 1C. The ultra-long stable cycling performance and excellent rate performance of LNT@SC-NMC532 stem from the small interfacial resistance and high ionic conductivity of the interfacial coating layer LNTO.^[11b,12]

The electrochemical performance validated that interfacial reactions between bare SC-NMC532 and LGPS can be suppressed by an interfacial coating of LNTO. However, the slow capacity decay is still observed after long cycling. To explore the interfacial reaction mechanism in greater detail and understand the interfacial evolution between LNT@SC-NMC532 and LGPS after many cycling, XPS was performed and results are analyzed in Figure 3.

Figure 3a shows the full surveys of pristine LGPS, bare SC-NMC532/LGPS after 100 cycles, in which the elements P, S, Ge, Ni, Co, and Mn are detected. S 2p and P 2p peaks of bare SC-NMC532/LGPS and LNT@SC-NMC532 change considerably after cycling (highlighted in yellow). The high-resolution S 2p spectra of pristine LGPS only show a pair of peaks at 161.26 eV that is from PS_4^{3-} (Figure 3b). Comparatively, bare SC-NMC532/LGPS after 100 cycles shows many additional peaks at higher binding energies. The peaks between 162 and 165 eV are assigned to polysulfides ($-\text{S}_n-$, $n \geq 2$) and elemental sulfides (S^0).^[9a,13] Additionally, prominent peaks at 166.8 and 168.8 eV are identified, which correspond to sulfates SO_3^{2-} and SO_4^{2-} , respectively.^[9a,14] With the LNTO interfacial coating layer, the relative contents of SO_4^{2-} and SO_3^{2-} peaks are significantly

decreased from 22.72% to 11.06% (Table S1, Supporting Information). However, the relative contents of peaks related to polysulfides and elemental sulfur (between 162 and 165 eV) almost keep no change (30.98% to 30.38%). This semi-quantification analysis implies that the non-oxygen species (i.e., polysulfides and elemental sulfur) that are electrochemically oxidized cannot be suppressed by interfacial coatings because of the narrow electrochemical window (1.7–2.1 V) of SEs.^[15] Figure 3c presents high-resolution P 2p spectra. Compared with the P 2p spectra of pristine LGPS, the P 2p spectrum of SC-NMC532/LGPS shows additional peaks at higher binding energy that are characteristic of PO_4^{3-} . Similarly, the intensity of P–O peaks is decreased with the LNTO interfacial coating. XPS analysis convincingly suggests that chemically formed oxygen-containing species (e.g., SO_4^{2-} , SO_3^{2-} , and PO_4^{3-}) can be effectively suppressed by interfacial coatings while electrochemically induced species (e.g., polysulfides, S_8) cannot.

It should be mentioned here that these oxygen-containing species are frequently observed at the interface between various oxide cathodes and sulfide electrolytes, such as LCO/LGPS,^[9a,16] LCO/ $\text{Li}_6\text{PS}_5\text{Cl}$,^[17] NMC811/ $\text{Li}_6\text{PS}_5\text{Cl}$,^[9b] and NMC811/ Li_3PS_4 .^[18] However, the underlying reason for the presence of these interfacial oxygen-containing species has never been clarified. In our case, we also found that the Mn 2p spectrum of SC-NMC532 after 100 cycles is shifted to lower binding energy in comparison with the Mn 2p spectrum of the bare SC-NMC532 in which the oxidation state of Mn is 4+, which indicates that Mn^{4+} of SC-NMC532 was reduced after long cycling (Figure 3d). The reduction of Mn^{4+} is also confirmed by electron energy loss spectroscopy (EELS) and XAS in Figures S4 and S5 (Supporting Information). With the interfacial LNTO coating, Mn reduction can be mitigated. Considering that the Mn^{4+} reduction of layered oxide cathodes is normally accompanied by oxygen loss

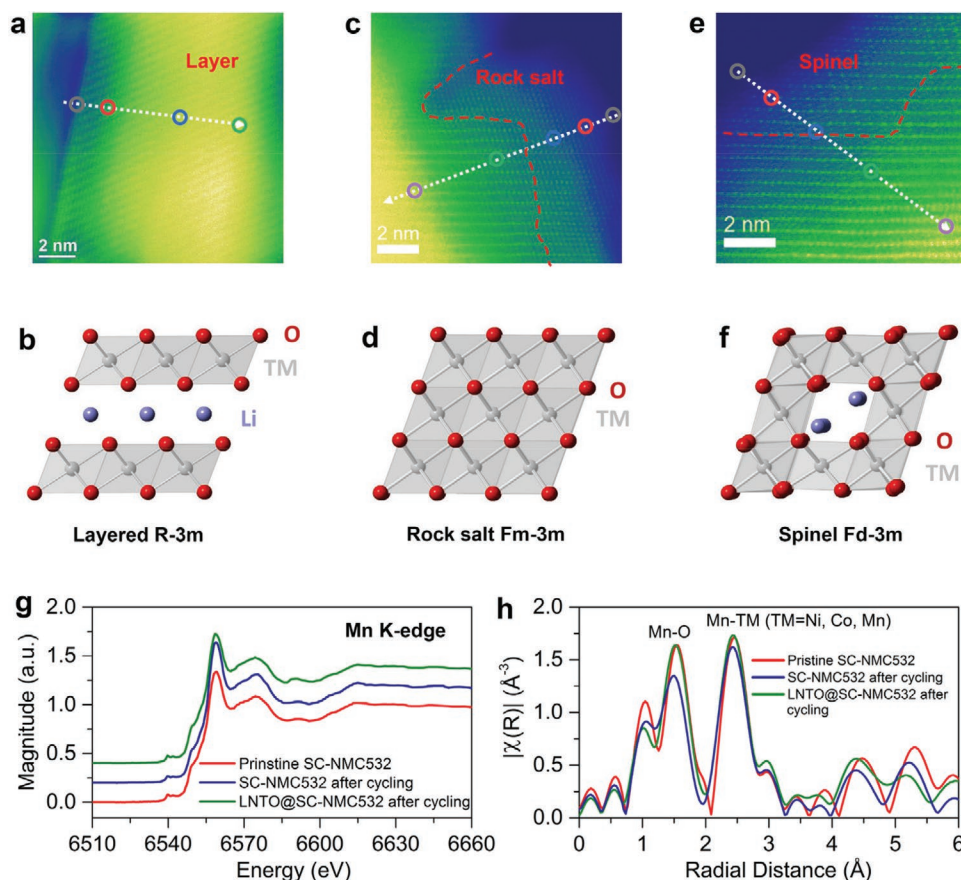


Figure 4. Interfacial structure change and chemical evolution of SC-NMC532. a) HAADF-STEM image of pristine SC-NMC532. b) HAADF-STEM image of SC-NMC532 after 100 cycles. c) HAADF-STEM image of LNT@SC-NMC532 after 100 cycles. d) Illustration of a layered R-3m structure. e) Illustration of a spinel Fd-3m structure. f) Illustration of a rock-salt structure. g) Mn K-edge XAS spectra and h) Mn K-edge EXFAS spectra ($k = 3\text{--}10.667 \text{ \AA}^{-1}$) of pristine SC-NMC532, SC-NMC532 after 100 cycles, and LNT@SC-NMC532 after 100 cycles.

from layered NMC oxide cathodes,^[19] it is natural to believe that the interfacial oxygen loss of SC-NMC532 reacts with LGPS, chemically forming oxygen-containing species (e.g., SO_3^{2-} , SO_4^{2-} , PO_4^{3-}) at the interface, which is also consistent with the theoretical prediction.^[20]

To verify this assumption, high-angle annular dark-field scanning transmission electron microscope (HAADF-STEM) images were acquired to observe interfacial structural changes of SC-NMC532. It should be mentioned that our TEM samples were rinsed by ethanol before transferring to TEM vacuum chambers to avoid the contamination of SEs, which are volatile under high-energy electron beams.

As displayed in Figure 4a, SC-NMC532 possesses a well-defined, layered structure corresponding to a layered R-3m structure (Figure 4b). The layered interfacial structure of SC-NMC532 was restructured to a rock-salt structure after 100 cycles (Figure 4c), which is caused by the interfacial oxygen loss and coincident interfacial reaction as well as the delithiation at the high voltage.^[21] It has been calculated by the first-principles theory that the rock-salt phase is thermodynamically favorable to form when more than 40% Li was removed from the NMC structure.^[21] Unlike the layered R-3m structure, the rock-salt structure is not beneficial for Li^+ transport (Figure 4d).^[19b,22] Therefore, this structural reconstruction

impedes the interfacial Li^+ transport between bare SC-NMC532 and LGPS, which also helps explain the large interfacial resistance of SE-based ASSLBs. This opinion has never been highlighted in previous studies.^[23] It should be emphasized here that both the interfacial reactions and near-surface structural change of oxide cathodes account for the large resistance of SE-based ASSLBs. Besides, a STEM-EELS line scan of the Mn $L_{2,3}$ edge is consistent with XPS results showing that the oxidation state of Mn is significantly reduced compared to that of pristine samples (Figure S4, Supporting Information), which also hints at the surface reconstruction of SC-NMC532 after cycling. With the LNTO interfacial coating, Mn reduction is alleviated (Figure S4, Supporting Information). Also, a spinel layer with a thickness of 1–3 nm was found on the surface of the LNTO@SC-NMC532 (Figure 4e). Considering that the average oxidation state of transition metals in the spinel structure is higher than that in the rock-salt structure (Figure S4e,f, Supporting Information), the surface coating can mitigate the detrimental interfacial structural change through the suppression of interfacial oxygen loss. The near-surface structural reconstruction and Mn reduction are closely associated with interfacial oxygen loss from SC-NMC532,^[21,24] which explains the oxygen-containing species (e.g., SO_4^{2-} , SO_3^{2-} , and PO_4^{3-}) at the interface between SC-NMC532 and LGPS.

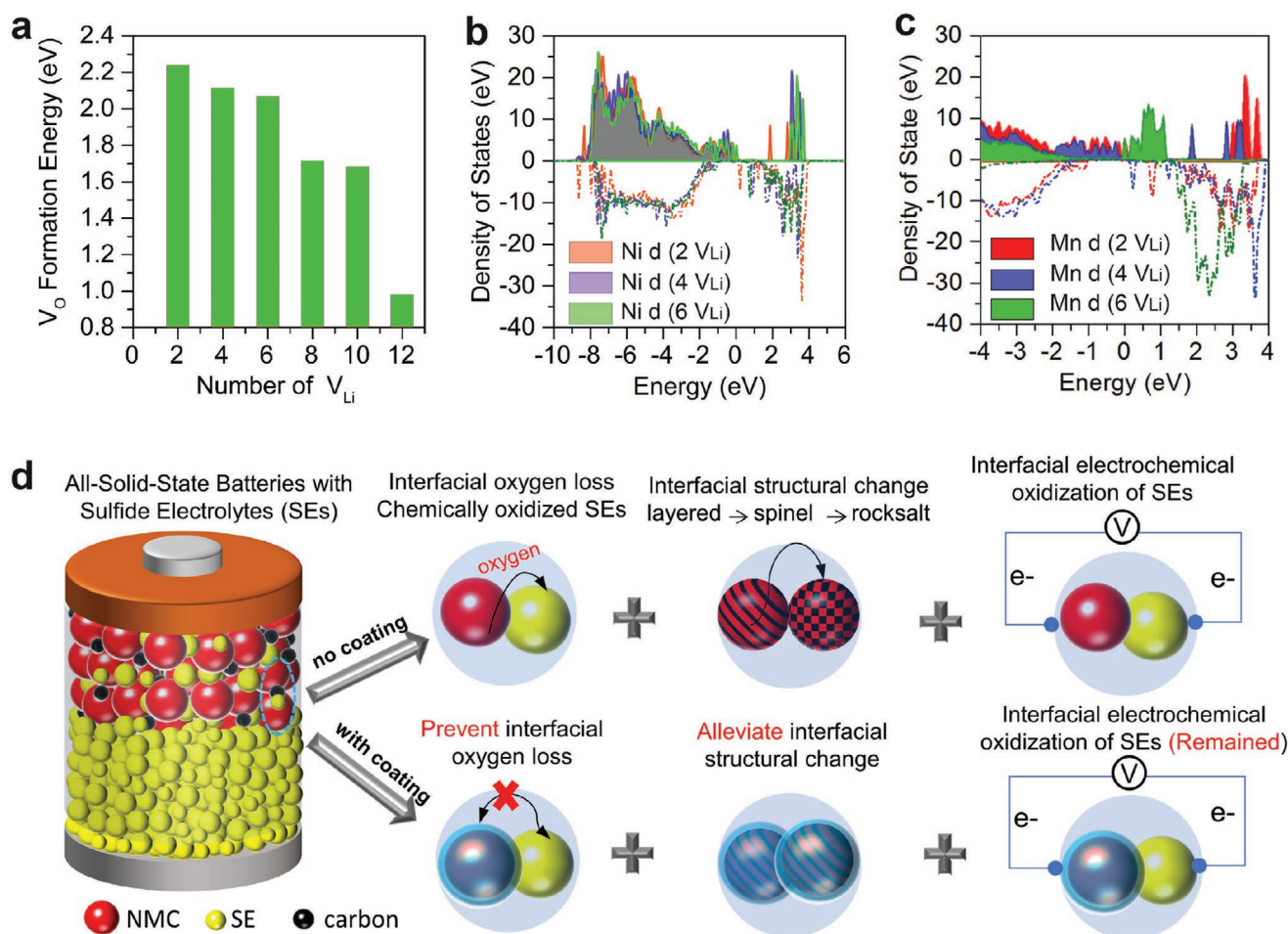


Figure 5. First-principles calculation to determine the formation energy of oxygen vacancies in SC-NMC532. a) The formation energy of oxygen vacancies with a function of Li vacancy numbers. b) The comparison of Ni d states after removing Li atoms from the supercell. c) The comparison of Mn d states after removing Li atoms from the supercell. The Fermi level was set to be 0 eV. d) Schematic illustration of the interfacial reaction mechanism and effects of the interfacial coating strategy.

Furthermore, XAS was performed to determine the oxidation state of transition metals of bare SC-NMC532, SC-NMC532 after 100 cycles, and LNT@SC-NMC532 after 100 cycles (Figure S5, Supporting Information).^[25] The Mn K-edge of bare SC-NMC532 after 100 cycles is located at a lower energy in comparison with that of pristine SC-NMC532, implying that Mn^{4+} is reduced after cycling (Figure 4g and Figure S5a,b, Supporting Information). With the LNT coating, Mn reduction was mitigated. Furthermore, extended X-ray absorption fine structure (EXAFS) spectra of Mn-K-edge obtained by Fourier transform are shown in Figure 4h. The first peak at 1.53 Å corresponds to the Mn–O shell while the second peak at 2.45 Å corresponds to Mn–TM (TM = Ni, Co, Mn) shell.^[26] Comparatively, the peak intensity of bare SC-NMC532 after electrochemical cycling is reduced, which explains the loss of Mn–O bonds.^[27] The slight difference in the radial distance is related to the structural evolution upon cycling. XAS profiles of the Co K-edge at 7730 eV do not show obvious change after cycling (Figure S5c,d, Supporting Information), suggesting that no obvious Li/Ni cationic mixing occurred during cycling.^[28] That explains the high electrochemical reversibility of LNT@SC-NMC532-

based ASSLBs, which can be cycled for up to 500 with excellent capacity retention. The slight peak shift in Ni K-edge profiles is related to the irreversible capacity loss after 100 cycles (Figure S5e,f, Supporting Information). The XAS results provide further evidence on the interfacial oxygen loss of SC-NMC532 in SE-based ASSLB, which induces the interfacial structural reconstruction of layered oxide cathodes.

Density functional theory (DFT) calculations were carried out to estimate the energetics of oxygen vacancy (V_O) formation in SC-NMC532 and its dependence on Li vacancy concentration (V_{Li}). In general, Li vacancies (V_{Li}) are generated during the charging and discharging of SC-NMC532. Oxygen vacancies (V_O) are associated with interfacial oxygen loss. **Figure 5a** shows the V_O formation energy as a function of V_{Li} . Surprisingly, the V_O formation energy reduces significantly when Li vacancies are generated in the lattices (during cycling), indicating that the generation of V_O in SC-NMC532 becomes increasingly favorable with the continued formation of V_{Li} (under high voltage). For example, with 12 V_{Li} , the formation energy of V_O is only 0.981 eV, which is far lower than the V_O formation energy at the pristine state (2.05 eV) (Figure S6,

Supporting Information). Besides, the d states in Ni shift to higher energy with the generation of Li vacancies, suggesting that the Ni^{2+} in the pristine SC-NMC532 is oxidized upon delithiation (Figure 5b). This observation is consistent with the fact that delithiation of NMC cathodes is accompanied by $\text{Ni}^{2+}/\text{Ni}^{4+}$ and $\text{Ni}^{3+}/\text{Ni}^{4+}$ oxidation.^[26b] On the contrary, the d states in Mn shift toward lower energy levels with the generation of Li vacancies (Figure 5c), suggesting that Mn tends to be reduced with the interfacial oxygen loss. This observation is fully consistent with the Mn XPS and XAS results discussed above. The DFT calculation results further demonstrate that interfacial oxygen loss in SC-NMC532 at high charging states is thermodynamically favorable, which also induces structure change of SC-NMC532.

3. Discussion

In this work, we deciphered the obscure interfacial chemical and electrochemical reactions between typical LGPS and layered oxide cathodes by a comprehensive analysis of XPS, HRTEM, XAS, and DFT calculation. The following conclusions can be drawn from the present study and schematically highlighted in Figure 5d. First, we revealed for the first time that interfacial oxygen loss from the layered oxide cathode significantly oxidizes SEs, chemically generating oxygen-containing species (e.g., SO_3^{2-} , SO_4^{2-} , PO_4^{3-}) at the interface. The interfacial oxygen loss also induces a structural change of oxide cathodes from a layered structure to a rock-salt structure. Second, the high operation voltage (2.5–4.4 V vs Li^+/Li) beyond the electrochemical window of SEs (1.7–2.1 V vs Li^+/Li) can induce the formation of non-oxygen interfacial species like polysulfides and elemental sulfur. Both the highly oxidized species and interfacial structural change (layered-to-rock salt) account for the large interfacial resistance in SE-based ASSLBs. Third, the widely adopted interfacial coating strategy is effective in suppressing chemically oxidized species (i.e., SO_3^{2-} , SO_4^{2-} , PO_4^{3-}) and interfacial structural change but is unable to prevent the formation of electrochemically induced species (e.g., polysulfides, S_8). Last but not least, LNT@SC-NMC532 exhibited a high reversible capacity of 161.4 mAh g^{-1} , which was retained at 88.6 mAh g^{-1} at C/3 after 500 cycles. A high capacity of 104.7 mAh g^{-1} was also achieved at 1C. The electrochemical performance is comparable to conventional lithium-ion batteries based on organic liquid electrolytes. This study provides a deeper insight into the large interfacial resistance between SE and oxide cathodes, which may be of assistance to the rational interface design of SE-based ASSLBs in future.

4. Experimental Section

Surface Modification of SC-NMC532: Stoichiometric amounts of lithium acetate (LiCO_2CH_3 , Sigma-Aldrich, 99.99%), niobium(V) ethoxide ($\text{Nb}(\text{OCH}_2\text{CH}_3)_5$, Sigma-Aldrich, 99.95%, trace metals basis), and tantalum(V) butoxide ($\text{Ta}(\text{OCH}_2\text{CH}_2\text{CH}_2\text{CH}_3)_5$, Sigma-Aldrich, 99.99%, trace metals basis) were dissolved in absolute ethanol (Sigma-Aldrich, >99.8%, GC) and stirred magnetically for 2 h. The mass fraction of LNTO sol-gel in absolute ethanol was diluted to 10%. 2 g of single-crystal $\text{LiNi}_{0.5}\text{Mn}_{0.3}\text{Co}_{0.2}\text{O}_2$ (SC-NMC532) (supplied from the China

Automotive Battery Research Institute) was dispersed into 5 mL of absolute ethanol. 2 wt% LNTO was then added to the SC-NMC532 solution. After magnetically stirring for 2 h, the solution was dried at 80 °C. The powder was further dried under vacuum at 100 °C overnight and annealed in air at 450 °C for 2 h. The samples are identified as LNTO@NMC532.

Characterizations: TEM was performed with a JEM-2100 operated at 200 kV. STEM-energy-dispersive spectroscopy (EDS) mapping was done with an FEI Talos F200X TEM (operated at 200 keV) equipped with an energy-dispersive X-ray spectrometer. HAADF-STEM imaging and EELS analysis were performed with a Hitachi HD2700C with a probe corrector. Scanning electron microscope (SEM) images were recorded with an SEM-4800. Powder X-ray diffraction (XRD) patterns were collected on a Bruker AXS D8 Advance with $\text{Cu K}\alpha$ radiation ($\lambda = 1.54178 \text{ \AA}$), and a special holder was used to avoid exposure to air during tests. XPS data were collected with a monochromatic Al $\text{K}\alpha$ source (1486.6 eV) using a Kratos AXIS Nova Spectrometer. X-ray absorption near edge structure (XANES) measurements were carried out at the Canadian Light Source (CLS). Mn K-edge XANES data were collected using fluorescence yield mode on the soft X-ray characterization beamline (SXRMB) at the CLS30. To avoid effects from air exposure, all samples were sealed with Mylar film attached to Al film.

Assembly of All-Solid-State Lithium-Ion Batteries: 70 mg of LNTO@SC-NMC532 and 30 mg of commercial LGPS (purchased from MSE supplies) were mixed to serve as the cathode composite. 80 mg of LGPS was first pressed at 1 ton. Then cathode composites were then uniformly spread on one side of the LGPS layer and pressed at 3.5 tons. An air blower was used to blow out unsettled powers. The remained mass loading of cathode composites is about 12 mg cm^{-2} . The relative density of the cathode composites is 3.07 g cm^{-3} . A piece of indium foil (with lithium foils) was placed on the other side of the LGPS and pressed at 0.5 ton. 50 MPa pressure was added during the cycling. The battery was rested for 3 h before electrochemical testing. The mass loading of NMC532 was 8.4 mg cm^{-2} . The theoretical discharge capacity of NMC532 is assumed to be 160 mAh g^{-1} . The areal capacity of electrodes is $\approx 1.344 \text{ mAh cm}^{-2}$. The current density of 1C is defined as 1.344 mA cm^{-2} . All-solid-state batteries were tested between 2.5 and 4.4 V (vs Li^+/Li) at room temperature by a LAND electrochemical analysis system. The electrochemical impedance spectra were recorded from 7 MHz to 0.1 Hz with an amplitude of 10 mV.

DFT Calculations: All calculations were carried out within the DFT framework as implemented in the Vienna Ab Initio Simulation Package (VASP). The projector augmented wave pseudopotentials were used to describe the interaction between ions and electrons, and exchange-correlation effects were treated using the Perdew–Burke–Ernzerhof (PBE) functional under the generalized gradient approximation (GGA) (generalized gradient approximation made simple). Herein, the electronic configurations for the PAW potentials were 1s2 2s1 for Li, 2s2 2p4 for O, 3d8 4s1 for Co, 3d9 4s1 for Ni, and 3d6 4s1 for Mn. The cutoff energy of the plane waves was 500 eV, and the Brillouin zone integrations were performed using a Monkhorst–Pack scheme with a $2 \times 2 \times 2$ k-point mesh (special points for Brillouin zone integrations). For the $\text{LiNi}_{0.5}\text{Mn}_{0.3}\text{Co}_{0.2}\text{O}_2$ structure, a Python program was used to generate 30 different configurations based on a $5 \times 2 \times 1$ supercell consisting of 120 atoms and determine the most energetically stable configuration by structural optimization. Ab initio molecular dynamics (AIMD) simulations were also performed to ascertain thermodynamic stabilities of NMC532 structures. AIMD simulations were carried out at 300 K using the Nose thermostat over 2 ps (a unified formulation of the constant temperature molecular dynamics methods). For the density of state (DOS) calculations, a DFT+U method was adopted to model the Coulombic repulsion between localized electrons in transition metals (first-principles calculations of the electronic structure and spectra of strongly correlated systems: the LDA+U method). The optimized values of Hubbard U values for Ni, Mn, and Co were taken as found to be 6.7, 4.2, and 4.91 eV, respectively, based on the previous study.^[29] The energy and force convergence limits were set to be 1×10^{-5} eV/atom and 1×10^{-5} eV \AA^{-1} , respectively. The VESTA package was used to visualize the

different structures (VESTA: a 3D visualization system for electronic and structural analysis).

Supporting Information

Supporting Information is available from the Wiley Online Library or from the author.

Acknowledgements

This work was supported by Natural Sciences and Engineering Research Council of Canada (NSERC), Canada Research Chair Program (CRC), Canada Foundation for Innovation (CFI), Ontario Research Fund, China Automotive Battery Research Institute Co., Ltd., Glabat Solid-State Battery Inc., the Canada Light Source at University of Saskatchewan (CLS), and University of Western Ontario. J.L. and X.L. thank the support of Mitacs Elevate Postdoctoral Fellowship. C.W. appreciates the funding support of Mitacs Accelerate Fellowship. This research used resources of the Center for Functional Nanomaterials, which is a U.S. DOE Office of Science Facility, at Brookhaven National Laboratory under Contract No. DE-SC0012704.

Conflict of Interest

The authors declare no conflict of interest.

Author Contributions

C.W., S.H., and M.J. contributed equally to this work. X.S. supervised the whole project. C.W. conceived the idea and designed all the experiments and characterizations. M.J., S.M., and C. V. S. conducted the first-principles calculations. S.H. and D.S. helped with TEM characterization and analysis. J.L. and X.L. interpreted the experimental results. Y.S. and K.A. helped with synchrotron characterizations. R.L. helped with purchasing all the chemicals. H.H., S.Z., L.Z., S.L., and J.W. interpreted data. C.W. wrote the manuscript, and M.Z. polished the language. C.V.S. acknowledges support from NSERC and Compute Canada. All the authors discussed the results and commented on the manuscript.

Data Availability Statement

The data supporting the findings of this study are available from the corresponding author upon request.

Keywords

all-solid-state lithium batteries, interfacial coating, interfacial oxygen loss, $\text{Li}_{10}\text{GeP}_2\text{S}_{12}$, single-crystal $\text{LiNi}_{0.5}\text{Mn}_{0.3}\text{Co}_{0.2}\text{O}_2$

Received: January 19, 2021
Revised: March 13, 2021
Published online: May 6, 2021

- [1] a) J. Janek, W. G. Zeier, *Nat. Energy* **2016**, *1*, 16141; b) Y. Kato, S. Hori, T. Saito, K. Suzuki, M. Hirayama, A. Mitsui, M. Yonemura, H. Iba, R. Kanno, *Nat. Energy* **2016**, *1*, 16030; c) Y.-G. Lee, S. Fujiki, C. Jung, N. Suzuki, N. Yashiro, R. Omoda, D.-S. Ko, T. Shiratsuchi, T. Sugimoto, S. Ryu, J. H. Ku, T. Watanabe, Y. Park, Y. Aihara, D. Im, I. T. Han, *Nat. Energy* **2020**, *5*, 299.

- [2] A. Miura, N. C. Rosero-Navarro, A. Sakuda, K. Tadanaga, N. H. H. Phuc, A. Matsuda, N. Machida, A. Hayashi, M. Tatsumisago, *Nat. Rev. Chem.* **2019**, *3*, 189.
[3] a) C. Wang, K. Fu, S. P. Kammampata, D. W. McOwen, A. J. Samson, L. Zhang, G. T. Hitz, A. M. Nolan, E. D. Wachsman, Y. Mo, V. Thangadurai, L. Hu, *Chem. Rev.* **2020**, *120*, 4257; b) M. Jia, N. Zhao, H. Huo, X. Guo, *Electrochem. Energy Rev.* **2020**, *3*, 656.
[4] J. Zhang, J. Zhao, L. Yue, Q. Wang, J. Chai, Z. Liu, X. Zhou, H. Li, Y. Guo, G. Cui, L. Chen, *Adv. Energy Mater.* **2015**, *5*, 1501082.
[5] a) T. Asano, A. Sakai, S. Ouchi, M. Sakaida, A. Miyazaki, S. Hasegawa, *Adv. Mater.* **2018**, 1803075; b) S. Wang, Q. Bai, A. M. Nolan, Y. Liu, S. Gong, Q. Sun, Y. Mo, *Angew. Chem., Int. Ed.* **2019**, *58*, 8039; c) L. Zhou, C. Y. Kwok, A. Shyamsunder, Q. Zhang, X. Wu, L. F. Nazar, *Energy Environ. Sci.* **2020**, *13*, 2056; d) J. Liang, X. Li, S. Wang, K. R. Adair, W. Li, Y. Zhao, C. Wang, Y. Hu, L. Zhang, S. Zhao, S. Lu, H. Huang, R. Li, Y. Mo, X. Sun, *J. Am. Chem. Soc.* **2020**, *142*, 7012; e) X. Li, J. Liang, X. Yang, K. R. Adair, C. Wang, F. Zhao, X. Sun, *Energy Environ. Sci.* **2020**, *13*, 1429.
[6] G. Sahu, Z. Lin, J. Li, Z. Liu, N. Dudney, C. Liang, *Energy Environ. Sci.* **2014**, *7*, 1053.
[7] J. Liang, N. Chen, X. Li, X. Li, K. R. Adair, J. Li, C. Wang, C. Yu, M. N. Banis, L. Zhang, S. Zhao, S. Lu, H. Huang, R. Li, Y. Huang, X. Sun, *Chem. Mater.* **2020**, *32*, 2664.
[8] X. Sun, A. M. Stavola, D. Cao, A. M. Bruck, Y. Wang, Y. Zhang, P. Luan, J. W. Gallaway, H. Zhu, *Adv. Energy Mater.* **2020**, *11*, 2002861.
[9] a) W. Zhang, F. H. Richter, S. P. Culver, T. Leichtweiss, J. G. Lozano, C. Dietrich, P. G. Bruce, W. G. Zeier, J. Janek, *ACS Appl. Mater. Interfaces* **2018**, *10*, 22226; b) J. Zhang, C. Zheng, L. Li, Y. Xia, H. Huang, Y. Gan, C. Liang, X. He, X. Tao, W. Zhang, *Adv. Energy Mater.* **2019**, *10*, 1903311; c) X. Li, Z. Ren, M. N. Banis, S. Deng, Y. Zhao, Q. Sun, C. Wang, X. Yang, W. Li, J. Liang, X. Li, Y. Sun, K. Adair, R. Li, Y. Hu, T.-K. Sham, H. Huang, L. Zhang, S. Lu, J. Luo, X. Sun, *ACS Energy Lett.* **2019**, *4*, 2480.
[10] D. Cao, Y. Zhang, A. M. Nolan, X. Sun, C. Liu, J. Sheng, Y. Mo, Y. Wang, H. Zhu, *Nano Lett.* **2020**, *20*, 1483.
[11] a) G. Qian, Y. Zhang, L. Li, R. Zhang, J. Xu, Z. Cheng, S. Xie, H. Wang, Q. Rao, Y. He, Y. Shen, L. Chen, M. Tang, Z.-F. Ma, *Energy Storage Mater.* **2020**, *27*, 140; b) C. Wang, R. Yu, S. Hwang, J. Liang, X. Li, C. Zhao, Y. Sun, J. Wang, N. Holmes, R. Li, H. Huang, S. Zhao, L. Zhang, S. Lu, D. Su, X. Sun, *Energy Storage Mater.* **2020**, *30*, 98; c) X. Liu, B. Zheng, J. Zhao, W. Zhao, Z. Liang, Y. Su, C. Xie, K. Zhou, Y. Xiang, J. Zhu, H. Wang, G. Zhong, Z. Gong, J. Huang, Y. Yang, *Adv. Energy Mater.* **2021**, *11*, 2003583.
[12] a) C. Wang, J. Liang, S. Hwang, X. Li, Y. Zhao, K. Adair, C. Zhao, X. Li, S. Deng, X. Lin, X. Yang, R. Li, H. Huang, L. Zhang, S. Lu, D. Su, X. Sun, *Nano Energy* **2020**, *72*, 104686; b) D. Cao, Y. Zhang, A. M. Nolan, X. Sun, C. Liu, J. Sheng, Y. Mo, Y. Wang, H. Zhu, *Nano Lett.* **2019**, *20*, 1483; c) Z. Jiang, S. Wang, X. Chen, W. Yang, X. Yao, X. Hu, Q. Han, H. Wang, *Adv. Mater.* **2020**, *32*, 1906221.
[13] a) S. Deng, X. Li, Z. Ren, W. Li, J. Luo, J. Liang, J. Liang, M. N. Banis, M. Li, Y. Zhao, X. Li, C. Wang, Y. Sun, Q. Sun, R. Li, Y. Hu, H. Huang, L. Zhang, S. Lu, J. Luo, X. Sun, *Energy Storage Mater.* **2020**, *27*, 117; b) D. H. S. Tan, E. A. Wu, H. Nguyen, Z. Chen, M. A. T. Marple, J.-M. Daux, X. Wang, H. Yang, A. Banerjee, Y. S. Meng, *ACS Energy Lett.* **2019**, *4*, 2418–2427; c) A. Y. Kim, F. Strauss, T. Bartsch, J. H. Teo, T. Hatsukade, A. Mazilkin, J. Janek, P. Hartmann, T. Brezesinski, *Chem. Mater.* **2019**, *31*, 9664.
[14] S. H. Jung, U.-H. Kim, J.-H. Kim, S. Jun, C. S. Yoon, Y. S. Jung, Y.-K. Sun, *Adv. Energy Mater.* **2020**, *10*, 1903360.
[15] F. D. Han, Y. Z. Zhu, X. F. He, Y. F. Mo, C. S. Wang, *Adv. Energy Mater.* **2016**, *6*, 1501590.
[16] C. Wang, X. Li, Y. Zhao, M. N. Banis, J. Liang, X. Li, Y. Sun, K. R. Adair, Q. Sun, Y. Liu, F. Zhao, S. Deng, X. Lin, R. Li, Y. Hu, T.-K. Sham, H. Huang, L. Zhang, R. Yang, S. Lu, X. Sun, *Small Methods* **2019**, *3*, 1900261.

- [17] J. Auvergniot, A. Cassel, J.-B. Ledeuil, V. Viallet, V. Seznec, R. Dedryvère, *Chem. Mater.* **2017**, 29, 3883.
- [18] R. Koerver, I. Aygün, T. Leichtweiß, C. Dietrich, W. Zhang, J. O. Binder, P. Hartmann, W. G. Zeier, J. Janek, *Chem. Mater.* **2017**, 19, 5574.
- [19] a) S.-K. Jung, H. Gwon, J. Hong, K.-Y. Park, D.-H. Seo, H. Kim, J. Hyun, W. Yang, K. Kang, *Adv. Energy Mater.* **2014**, 4, 1300787; b) S. Sharifi-Asl, J. Lu, K. Amine, R. Shahbazian-Yassar, *Adv. Energy Mater.* **2019**, 9, 1900551.
- [20] Y. Zhu, X. He, Y. Mo, *J. Mater. Chem. A* **2016**, 4, 3253.
- [21] F. Lin, I. M. Markus, D. Nordlund, T.-C. Weng, M. D. Asta, H. L. Xin, M. M. Doeff, *Nat. Commun.* **2014**, 5, 3529.
- [22] S. Hu, A. S. Pillai, G. Liang, W. K. Pang, H. Wang, Q. Li, Z. Guo, *Electrochem. Energy Rev.* **2019**, 2, 277.
- [23] a) Q. Zhang, D. Cao, Y. Ma, A. Natan, P. Aurora, H. Zhu, *Adv. Mater.* **2020**, 31, 1901131; b) S. P. Culver, R. Koerver, W. G. Zeier, J. Janek, *Adv. Energy Mater.* **2019**, 0, 1900626; c) K. Takada, T. Ohno, N. Ohta, T. Ohnishi, Y. Tanaka, *ACS Energy Lett.* **2017**, 3, 98; d) D. H. S. Tan, A. Banerjee, Z. Chen, Y. S. Meng, *Nat. Nanotechnol.* **2020**, 15, 170; e) S. Chen, D. Xie, G. Liu, J. P. Mwizerwa, Q. Zhang, Y. Zhao, X. Xu, X. Yao, *Energy Storage Mater.* **2018**, 14, 58; f) R. Chen, Q. Li, X. Yu, L. Chen, H. Li, *Chem. Rev.* **2020**, 120, 6820.
- [24] a) J. Lee, J. K. Papp, R. J. Clément, S. Sallis, D.-H. Kwon, T. Shi, W. Yang, B. D. McCloskey, G. Ceder, *Nat. Commun.* **2017**, 8, 981; b) E. Hu, X. Yu, R. Lin, X. Bi, J. Lu, S. Bak, K.-W. Nam, H. L. Xin, C. Jaye, D. A. Fischer, K. Amine, X.-Q. Yang, *Nat. Energy* **2018**, 3, 690.
- [25] C. Tian, F. Lin, M. M. Doeff, *Acc. Chem. Res.* **2018**, 51, 89.
- [26] a) J. Lu, C. Zhan, T. Wu, J. Wen, Y. Lei, A. J. Kropf, H. Wu, D. J. Miller, J. W. Elam, Y.-K. Sun, X. Qiu, K. Amine, *Nat. Commun.* **2014**, 5, 5693; b) T. Li, X.-Z. Yuan, L. Zhang, D. Song, K. Shi, C. Bock, *Electrochem. Energy Rev.* **2020**, 3, 43.
- [27] S. Lee, W. Jin, S. H. Kim, S. H. Joo, G. Nam, P. Oh, Y.-k. Kim, S. K. Kwak, J. Cho, *Angew. Chem., Int. Ed.* **2019**.
- [28] S. S. Zhang, *J. Energy Chem.* **2020**, 41, 135.
- [29] R. Xu, H. Sun, L. S. de Vasconcelos, K. Zhao, *J. Electrochem. Soc.* **2017**, 164, A3333.